catalysts

MDPI

Review

Recent Advances in Electrochemical Nitrogen Reduction Reaction to Ammonia from the Catalyst to the System

Yong Hyun Moon [1,†], Na Yun Kim [1,†], Sung Min Kim [1] and Youn Jeong Jang [1,2,*]

[1] Department of Chemical Engineering, Hanyang University, 222 Wangsimni-ro, Seoul 04763, Korea
[2] Institute of Nano Science and Technology, Hanyang University, 222 Wangsimni-ro, Seoul 04763, Korea
* Correspondence: yjang53@hanyang.ac.kr
† These authors contributed equally to this work.

Abstract: As energy-related issues increase significantly, interest in ammonia (NH_3) and its potential as a new eco-friendly fuel is increasing substantially. Accordingly, many studies have been conducted on electrochemical nitrogen reduction reaction (ENRR), which can produce ammonia in an environmentally friendly manner using nitrogen molecule (N_2) and water (H_2O) in mild conditions. However, research is still at a standstill, showing low performances in faradaic efficiency (FE) and NH_3 production rate due to the competitive reaction and insufficient three-phase boundary (TPB) of N_2(g)-catalyst(s)-H_2O(l). Therefore, this review comprehensively describes the main challenges related to the ENRR and examines the strategies of catalyst design and TPB engineering that affect performances. Finally, a direction to further develop ENRR through perspective is provided.

Keywords: ammonia; nitrogen reduction reaction; electrocatalyst; system engineering; three-phase boundary

check for updates

Citation: Moon, Y.H.; Kim, N.Y.; Kim, S.M.; Jang, Y.J. Recent Advances in Electrochemical Nitrogen Reduction Reaction to Ammonia from the Catalyst to the System. *Catalysts* **2022**, *12*, 1015. https://doi.org/10.3390/catal12091015

Academic Editor: Eun Duck Park

Received: 14 August 2022
Accepted: 5 September 2022
Published: 7 September 2022

Publisher's Note: MDPI stays neutral with regard to jurisdictional claims in published maps and institutional affiliations.

Copyright: © 2022 by the authors. Licensee MDPI, Basel, Switzerland. This article is an open access article distributed under the terms and conditions of the Creative Commons Attribution (CC BY) license (https://creativecommons.org/licenses/by/4.0/).

1. Introduction

Ammonia (NH_3) is an essential commodity for chemicals utilized in various industries, such as fertilizers, plastics, dyes, pharmaceuticals, and so on [1,2]. In particular, its use as a fertilizer made mass production of food possible and led to a population increase. Recently, NH_3 has been focused on as a sustainable fuel and a hydrogen storage medium with the promising properties of 5.52 kWh kg^{-1} high energy density and 17.6% high hydrogen content [3]. According to the US Geological Survey, NH_3 production in 2021 has gradually increased to as much as 150 million tons [4].

Most NH_3 production mainly relies on the traditional Haber–Bosch process which converts hydrogen (H_2) and nitrogen (N_2) directly into NH_3 ($N_2 + 3H_2 \rightleftharpoons 2NH_3$) using Fe-based catalysts [5]. However, since the Haber–Bosch process requires extreme operating conditions—such as a temperature and pressure of over 400 °C and 20 MPa, respectively—to cleave the strong triple-bond energy (941 kJ mol^{-1}) of N_2 molecules, the process annually consumes a significant amount of energy accounting for around 1–3% of globally produced energy [6–9]. Furthermore, the requirement of the enormous H_2 supply generated by fossil fuels leads to significant carbon dioxide (CO_2) emissions, which amounted to 300 million tons [8]. When we convert it to an energy requirement per ton of NH_3 production, the theoretical energy requirement for the Haber–Bosch process is 22.2–28.8 GJ $t_{NH3}{}^{-1}$. Furthermore, CO_2 emission from the Haber–Bosch process is expected to be 1.673 t_{CO2} $t_{NH3}{}^{-1}$ [10,11]. Considering the increasing need for NH_3 and the Haber–Bosch process' economic and environmental issues, a novel environmentally friendly and economically efficient NH_3 production process is in high demand.

The electrochemical nitrogen reduction reaction (ENRR) is one of the most attractive NH_3 production processes. NH_3 can be produced using H_2O as a hydrogen source and N_2 gas at mild temperature and pressure under biased conditions. Theoretical minimum energy requirement for ENRR is expected to be only 19.9 GJ $t_{NH3}{}^{-1}$, as assuming ideal

1.17 V supplying for overall NH_3 production with 100% of faradaic efficiency. Furthermore, a negligible amount of CO_2 during ENRR is expected, if electricity supplied is from renewable energy such as wind and solar and the possibility of CO_2 emission from process engineering is excluded such as product separation, input gas compression, and so on [10,11]. Thus, ENRR can significantly reduce CO_2 emission and energy consumption compared to the Haber–Bosch process. However, ENRR has several critical challenges hindering its practical applications due to the insufficient performances recorded so far. For example, to apply the ENRR as a major NH_3 production pathway in industrial systems, an NH_3 production rate of at least 6120 μg h^{-1} cm^{-2} should be achieved [12,13]. However, despite great efforts for advancing the ENRR's performance, the NH_3 production rate is still significantly low with 612 μg h^{-1} cm^{-2} and a Faradaic efficiency (FE) below 10% [14]. Thus, it is critical to understand the ENRR's major limitations and the previous efforts of overcoming the challenges to propose the next generation of ENRR, which would be a practical available alternative to the Haber–Bosch pathway.

In this review, we will first discuss the essential ENRR thermodynamics fundamentals, kinetics related to reaction mechanisms, and other factors affecting the ENRR's performance. Next, we review the widely studied catalyst design strategies and reaction environmental engineering. Moreover, we will thoroughly investigate each strategy's effect on the ENRR's performance (Scheme 1). Finally, we end this review by showing ENRR's great prospects and the direction for further investigation to apply it in the future.

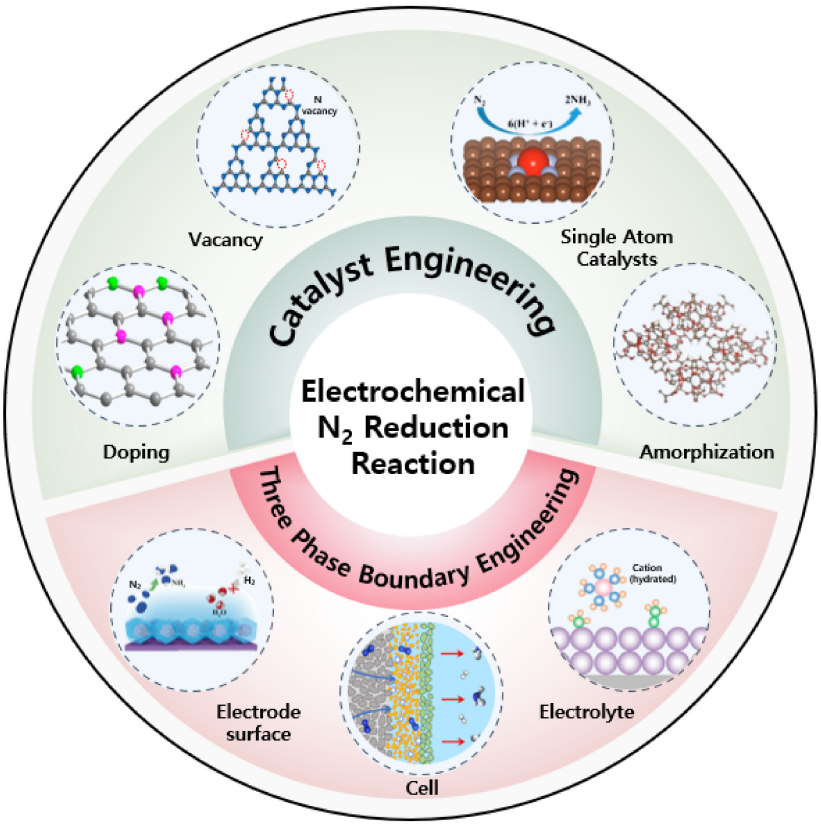

Scheme 1. Schematic diagram of electrochemical N_2 reduction reaction performance improvement strategies covered in this paper. Schematic of doping, reproduced with permission [15]. Copyright 2021, Elsevier B.V. Schematic of vacancy, reproduced with permission [16]. Copyright 2020, American Chemical Society. Schematic of single-atom catalysts, reproduced with permission [17]. Copyright 2018, American Chemical Society. Schematic of amorphization, reproduced with permission [18]. Copyright 2018, Wiley–VCH. Schematic of electrode surface, reproduced with permission [19]. Copyright 2019, Wiley–VCH. Schematic of cell, reproduced with permission [20]. Copyright 2020, American Chemical Society.

2. The Fundamentals

The ENRR is composed of multiple steps of proton-coupled electron transfers involving six protons and six electrons. The ENRR's half-reactions in acidic (1) and basic solutions (2) with standard reduction potential against reversible hydrogen evolution (RHE) reaction are given, respectively [14]

$$N_2(g) + 6H^+(aq) + 6e^- \rightleftharpoons 2NH_3(aq)\ (E^0 = 0.092\ V_{RHE}) \quad (1)$$

$$N_2(g) + 6H_2O(l) + 6e^- \rightleftharpoons 2NH_3 + 6OH^-(aq)\ (E^0 = 0.092\ V_{RHE}) \quad (2)$$

The Pourbaix diagram for N_2-H_2O in Figure 1a represents thermodynamically favored species and phases depending on potential and the solution's pH [3]. Thermodynamically, only the ENRR is available and thus FE for NH_3 must be 100% at the potential and pH within the yellow-colored area. This area is between the red solid line representing N_2 reduction to NH_4^+ or NH_3 and the line ⓐ representing the hydrogen evolution's reaction (HER, $2H^+(aq) + 2e^- \rightleftharpoons H_2(aq)$, $E^0 = 0.000\ V_{RHE}$). Furthermore, ENRR can be more favorable than HER at the potential below 0 V_{RHE}. However, the ENRR's performance is very poor in the yellow-colored area and the HER is more favorable than the ENRR at the potential below 0 V_{RHE}. The experimental observation can be supported by an additional challenge for the kinetic manner.

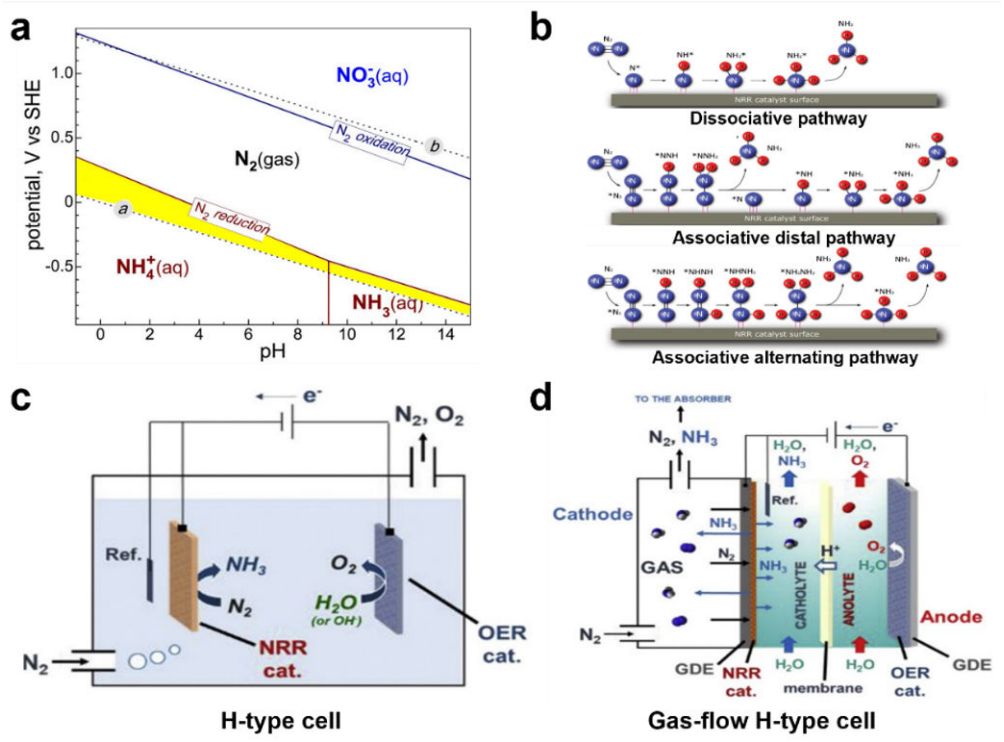

Figure 1. (**a**) Pourbaix diagram of nitrogen species, reproduced with permission [3]. Copyright 2018, The American Association for the Advancement of Science. (**b**) Schematic diagram of the N_2 reduction pathways, reproduced with permission [21]. Copyright 2019, Wiley–VCH. Reactor configurations of commonly used (**c**) H-type cell. Advanced cell configuration of (**d**) gas-flow H-type cell, reproduced with permission [22]. Copyright 2022, Elsevier B.V.

As shown in Figure 1b, pathways for N_2 to NH_3 conversion using six transferred electron and proton pairs are mainly represented as dissociative or associative steps [21]. In the dissociative pathway, the dissociated N atom is strongly adsorbed to the catalyst surface by the perfect cleavage of triple bonds from the N_2 molecule. Then, NH_3 is produced by multiple hydrogenations. However, this dissociative process is much more relatable to the NH_3 production via the Haber–Bosch process performed under high temperature

and pressure than the ENRR because the N_2 triple bonds cleavage requires enormous energy input. Meanwhile, the ENRR's mechanism is well-followed by the associative pathway where the first hydrogenation occurs with the adsorbed N_2 ($*N_2$), forming an $*N_2H$ intermediate [23]. The associative mechanism is further classified into two different pathways: the distal and alternating pathways. In the distal associative pathway, the N atom that is far from the catalyst's adsorption site is first hydrogenated with the three transferred electrons and protons and then released as NH_3. The other N atom still adsorbed on the catalyst conducts further hydrogenation to form NH_3. On the other hand, in the alternating pathway, the protons are alternately bonded with both N atoms until the final N-N bond is cleaved [14]. Finally, two NH_3 molecules are released. The initial step of N_2 adsorption and activation by forming the $*N_2H$ intermediate is a serious rate-determining step among the multiple steps for the ENRR. Furthermore, this multi-proton-coupled electron transfer process involves diverse intermediate formations, such as *NNH, $*NH_2$, and *NHNH with severe complexity. This results in sluggish kinetics relative to the HER, requiring a simple electron transfer with protons. Combining the thermodynamic and kinetic manner for the ENRR, a rational design of catalysts is critical for facilitating N_2 adsorption, activation, and selective NH_3 production with multiple byproduct evolution or competitive HER suppression.

The ENRR's performance is evaluated mainly using two factors of FE that represent the utilization ratio of the passed coulomb in NH_3 production and the production rate that shows the amount of NH_3 produced using a unit area (1 cm^2) of electrodes during an hour. The US Department of Energy (DOE) aims to achieve an FE of 50% for the ENRR and an NH_3 production rate of over 1700 μg h^{-1} cm^{-2} [24]. However, the FE and production rate typically trade off in most reports [25,26]. Therefore, the suitable three-phase boundary of N_2(g)-catalyst(s)-H_2O(l) with well-controlled mass transport of reactants and products, including catalyst engineering, is required to finally advance the NH_3 production rate [27]. The majority of ENRR has been performed in typical H-type cells, where the two compartments were separated with a membrane with a N_2 purging electrolyte as shown in Figure 1c [22,28,29]. However, since the N_2 gas solubility in H_2O is significantly low, reaching as low as 0.0126 $mg \cdot g^{-1}$, the effective three-phase boundary representing active sites is insufficient, resulting in a low ENRR performance [20]. Thus, a strategy of adjusting the N_2 and H_2O concentrations in catalysts needs to be suggested. For example, a proposed representative is promoting the N_2 concentration near the catalyst by directly supplying N_2 gas across a gas diffusion electrode (GDE) as shown in Figure 1d [22]. Like this strategy, diverse reaction environmental engineering is required to enhance performances. Considering the discussed ENRR fundamentals, the strategies to design catalysts and systems and their effect on the ENRR's performance will be reviewed in the next section.

3. Catalyst Engineering

Electrocatalysts for the ENRR have been developed using metals (Ag, Cu, W, Mo, Se, Fe, etc.), non-metals (Cl, B, F, P, S, O, N, etc.), metal oxides (TiO_2, $Bi_4V_2O_{11}$, etc.), metal sulfide (MoS_2), and carbon-based materials (graphdiyne, g-C_3N_4, N-doped carbon, etc.). In this section, we will review the representative strategies for ENRR improvement via facilitating N_2 activation and suppressing the competitive reaction.

3.1. Doping

Doping with atoms of different sizes and charge to the original electrocatalyst has been widely suggested in various electrocatalytic applications. The dopants can alter the electrocatalyst's electronic structure and change the binding strength of the reactant, intermediate, or product at active sites. Thus, they govern the electrocatalytic performance [30–33].

Recently, Qing Jiang et al. prepared Ag-doped Cu nanosheets cultivated on carbon paper (Ag-Cu_{ns}/CP) by a simple electrochemical deposition [34]. The prepared Ag-Cu_{ns}/CP exhibited a highly advanced ENRR compared to undoped Cu_{ns}/CP. For example, at

−0.4 V_{RHE} in 0.1 M of Na_2SO_4, the Ag-Cu_{ns}/CP catalyst showed an FE of 20.9% and an NH_3 production rate of 4.56 μg h^{-1} cm^{-2}, whereas Cu_{ns}/CP showed an FE of only 3.14% and an NH_3 yield rate of 2.28 μg h^{-1} cm^{-2}. As revealed by X-ray photoelectron spectroscopy (XPS) on the Ag-doped Cu nanosheets sample, as shown in Figure 2a, the binding energy of Cu^0 positively shifted compared to the pristine Cu nanosheets and that of Ag^0 was negatively shifted compared to bulk Ag particles. This indicates that electrons from Cu sheets were partially transferred into Ag dopants, resulting in the formation of electron-deficient Cu sites in Ag-Cu_{ns}/CP. The electron-deficient Cu sites prevent proton adsorption and simultaneously provide opportunities to accept lone-pair electrons of N_2 molecules due to the suitable overlapping of orbitals from N_2 and electron-deficient Cu. Consequently, the properties induced by Ag doping on the Cu nanosheets suppress the HER and facilitate ENRR.

Carbon-based metal-free catalysts have been receiving great attention due to their attractive properties, such as high surface area, excellent conductivity, easily controllable defects, and effective cost [35]. To utilize these characteristics, Lele Duan et al. suggested metal-free Cl-doped ultrathin graphdiyne (Cl-GDY) electrocatalysts prepared by annealing the pristine GDY precursors with Ar and Cl_2 gases [36]. At −0.45 V_{RHE} in 0.1 M HCl, the prepared Cl-GDY exhibited an FE of 8.7% and an NH_3 production rate of 10.7 μg h^{-1} cm^{-2}, whereas pristine GDY exhibited an FE of 2.5% and a NH_3 production rate of 3.02 μg h^{-1} cm^{-2}. Investigating the intensity ratio of the D to G band (I_D/I_G), representing the defect density and induced structural disordering of the carbon materials in Raman spectra revealed that the Cl-GDY exhibited a highly enhanced ratio compared with the pristine GDY. This implies that the Cl dopants increase defect sites, acting as active sites and structural distortions of GDY, resulting in improved ENRR performance.

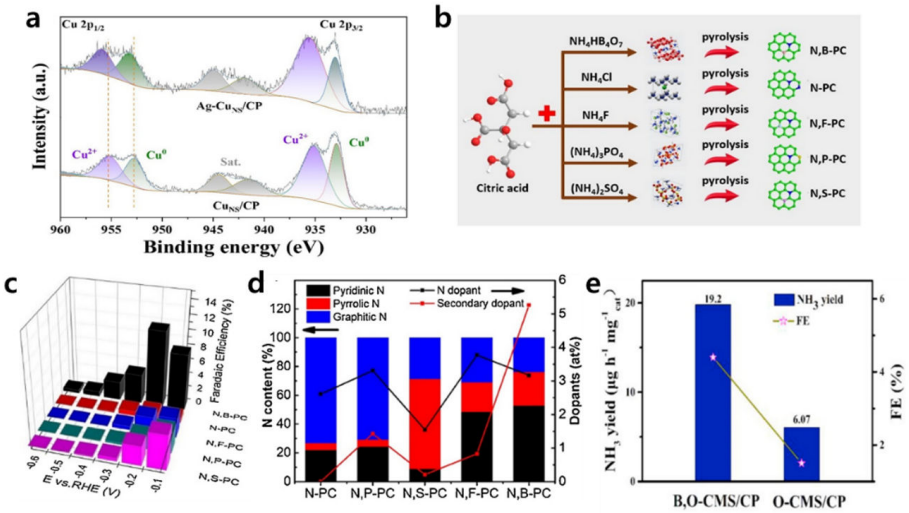

Figure 2. (**a**) Cu 2p XPS of Ag-Cu_{NS}/CP and Cu_{NS}/CP. Reproduced with permission [34]. Copyright 2021, Elsevier B.V. (**b**) Scheme of the heteroatoms co-doped porous carbons. (**c**) FEs of the heteroatoms co-doped porous carbons and N doped porous carbon. (**d**) Contents of total N and specific N species with secondary dopants. Reproduced with permission [37]. Copyright 2020, Elsevier B.V. (**e**) NH_3 production rate (NH_3 yield rates) and FEs of B,O-CMS/CP and O-CMS/CP. Reproduced with permission [15]. Copyright 2020, Elsevier B.V.

Furthermore, the synergistic effect of dual heteroatom doping for ENRR was reported using citric acid-derived carbon electrocatalysts. Zhong-Yong Yuan et al. prepared dual heteroatom doped porous carbon (PC) by combining N dopants with B, F, P, or S dopants as shown in Figure 2b [37]. Depending on the dopant's combination, their FEs were altered significantly as shown in Figure 2c. Among them, N, B-doped porous carbon (N,B-PC) exhibited the highest FE of 10.58% and an NH_3 production rate of 16.4 μg h^{-1} cm^{-2} at −0.2 V_{RHE} in 0.1 M HCl. The major contribution of dual dopants was investigated

using Raman spectroscopy. Considering the (I_D/I_G), all dual-doped PCs, N,B-PC (1.025), N,F-PC (1.006), N,P-PC (0.978), and N,S-PC (0.976) demonstrated an increased structural disordering compared with the single N doped PC (0.962). Furthermore, N and B dual doping, pyridinic N ratio, and providing active sites for strong adsorption for N_2 largely increased compared to others in the XPS N 1s spectra (Figure 2d). Those two results indicate that dual heteroatom doping can effectively control the disordering and electronic structure of electrocatalysts affecting N_2 activation on active sites, resulting in ENRR improvement.

Dunmin Lin et al. also prepared dual-doped electrocatalysts, B,O-co-doped carbon microspheres (B,O-CMS) via a hydrothermal method [15]. The prepared B,O-CMS achieved a two-fold enhanced FE of 5.57% and an almost triple NH_3 production rate of 1.92 μg h^{-1} cm^{-2} compared with O-CMS at −0.25 V_{RHE} in 0.1 M HCl as shown in Figure 2e. The B,O-CMS showed an increased I_D/I_G ratio of 0.93 compared to the single doped O-CMS (0.88) in Raman spectra, indicating that the B,O-CMS has more defect sites acting as active sites than the O-CMS. Furthermore, as revealed by the Brunauer–Emmett–Teller (BET) measurements, the B,O-CMS provided more surface area than the O-CMS, in which each B,O-CMS and O-CMS showed a surface area of 488.7 and 373.6 m^2 g^{-1}, respectively.

These reports demonstrated that the doping strategy can adjust key factors for the ENRR by developing defect sites, providing or inducing neighbor's active sites, ordering/disordering the shift, surface area, and so on.

3.2. Vacancy

Surface vacancy formation is one of the most used strategies for creating active sites for ENRR. Vacant sites can have abundant localized electrons to preserve charge neutrality. The enriched electrons can weaken the N_2 triple bond, resulting in facilitating the ENRR [38]. In this part, we will thoroughly review the progress on oxygen (O_v), nitrogen (N_v), and sulfur vacancies (S_v) derived from various electrocatalysts (TiO_2, C_3N_4, W_2N_3, and MoS_2).

The O_v formation has been the most developed strategy for ENRR, particularly for metal oxide-based electrocatalysts. Zhenyu sun et al. prepared O_v rich TiO_2 via a solvothermal method and then annealed at different temperatures of 700, 800, and 900 °C under Ar gas flow [39]. At −0.12 V_{RHE} in 0.1 M HCl, the O_v rich TiO_2 sample annealed at 800 °C achieved the highest FE of 6.5% and an NH_3 production rate of 3.6 μg h^{-1} cm^{-2} among others. For example, the pristine TiO_2 showed a low FE and NH_3 production rate (2.4% and 1.5 μg h^{-1} cm^{-2}, respectively). They conducted O 1s XPS measurements to investigate atomic compositions and their chemical states on the catalyst's surface. Each O_v rich TiO_2 sample, annealed at 700, 800, and 900 °C, was composed of O_v 18.4, 32.2, and 25.6%, respectively. Furthermore, the electron localized near the O_v sites managed to partially reduce the oxidation state of Ti^{4+}, which served as an active site for ENRR. As the annealing temperature increased from 700 to 800 °C, the O_v amount also increased. However, when the annealing temperature increased from 800 to 900 °C, the O_v amount decreased. This was mainly due to the unintentional crystal structure's change from original anatase to rutile over 800 °C. O_v formation is much more favored in the anatase phase relative to rutile [40]. As expected, the amount of reduced Ti^{4+} increased from 700 to 800 °C, but decreased from 800 to 900 °C in Ti 2p XPS. Those results reveal that reduced Ti^{4+} sites coupled with O_v were critical for the ENRR.

Jiantai Ma et al. prepared an N_2 vacant 2D C_3N_4 (2D C_3N_4-NV), showing good stability and a large specific surface area via annealing 2D C_3N_4 nanosheets at 600 °C under an N_2 gas flow for 15 min as shown in Figure 3a [41]. The prepared 2D C_3N_4-NV exhibited a highly advanced FE of 10.96% and an NH_3 production rate of 178.5 μg h^{-1} cm^{-2} at −0.30 V_{RHE} in 0.1 M HCl compared with pristine 2D C_3N_4 in Figure 3b. The dramatic performance advances by N_v formation were mainly due to the N_2 adsorption ability, which is regarded as the primary challenge for ENRR. Based on the N_2 adsorption–desorption isotherm measurements, the N_2 adsorption capacity of 2D C_3N_4-NV was 193.6 cm^3 g^{-1}, which is almost 2 times and 1.4 times better than that of bulk C_3N_4 (91.5 cm^3 g^{-1}) and 2D C_3N_4, respectively. Furthermore, density functional theory (DFT) calculations support

that electron-rich N_v sites can facilitate N_2 adsorption via weakening the N_2 triple bonds, resulting in a superior ENRR performance for 2D C_3N_4-NV.

Shi-zhang Qiao et al. prepared N_v on 2D layered W_2N_3 with excellent structural stability (NV-W_2N_3) by annealing $Na_2W_4O_{13}$ under an NH_3 gas flow [42]. The presence of N_v sites on W_2N_3 was revealed via XPS N 1s spectra, where N vacancy peaks at 400.2 eV could be observed in Figure 3c. Furthermore, in the extended X-ray absorption fine structure (EXAFS), NV-W_2N_3 showed a weakened W-N bonding, indicating a decreased W-N bonding number compared to pristine W_2N_3 in Figure 3d. The pristine W_2N_3 showed an FE of 3.5% and an NH_3 production rate of 0.94 μg h^{-1} cm^{-2} at −0.2 V_{RHE} in 0.1 M KOH. The ENRR performance was significantly improved by N_v formation, showing an FE of 11.67% and NH_3 production rate of 2.332 μg h^{-1} cm^{-2} at the same experimental condition as shown in Figure 3e. From the DFT calculation, it is revealed that electron-deficient W in W_2N_3 induced by N_v facilitates N_2 adsorption and lowers the thermodynamic limiting potential of ENRR.

Recently, strategies for inducing sulfur vacancies (S_v) have been widely proposed, such as O_v and N_v formation. The molybdenum disulfide (MoS_2), which is a representative electrocatalyst of HER, has been proposed as a catalyst for ENRR by S_v engineering [43,44]. Deliang Chen et al. developed S_v-rich MoS_2 by molybdenite precursors annealing at 800 °C (MoS_2-800) in an Ar gas flow [45]. As a result, the prepared MoS_2-S_v achieved an FE of 17.9% and an NH_3 production rate of 9.352 μg h^{-1} cm^{-2} at −0.35 V_{RHE} in 0.1 M HCl, showing twice and 3.5-times higher FE and NH_3 production rate for pristine MoS_2, respectively. The major contribution of S_v was revealed in the XPS spectra of Mo 3d, where the peak attributed to Mo^{4+} was positively shifted for MoS_2-800 compared with pristine MoS_2. On the other hand, in the XPS spectra of S 2p, the peaks attributing to S^{2-} were negatively shifted for MoS_2-800 relative to MoS_2. The peak shift of Mo implies electron transferring from Mo to other defect sites, whereas the peak shift of S implies the existence of deficient electrons. Additionally, the N_2 temperature-programmed desorption (N_2-TPD) results clearly exhibit the critical effect of S_v as shown in Figure 3e. The MoS_2-800 represents a much stronger N_2 physisorption peak at 98 °C and chemisorption peak at 385 °C compared to the pristine MoS_2, indicating that S_v in MoS_2-800 enhanced the N_2 adsorption ability. The progresses discussed in this part shows that vacancy engineering can effectively alter oxidation states around vacancies, affecting N_2 adsorption by weakening the N_2 triple bonds and increasing N_2 adsorption capacities, consequently enhancing ENRR.

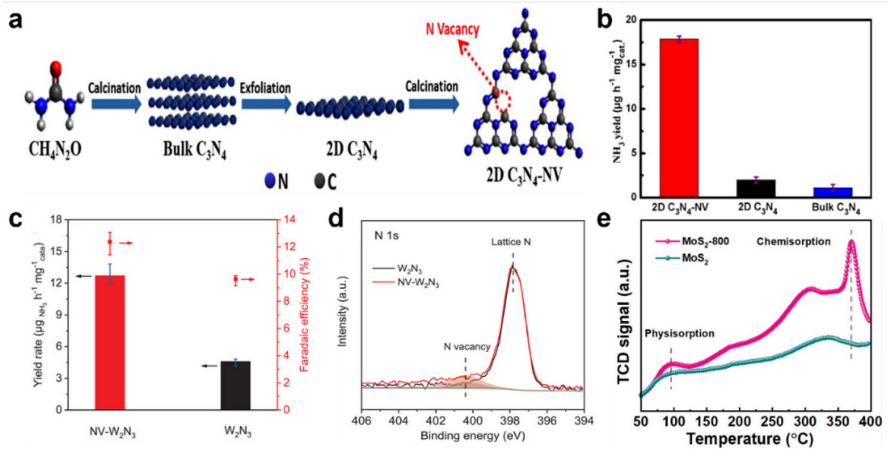

Figure 3. (**a**) Schematic diagram of 2D C_3N_4-NV synthetic route. (**b**) NH_3 production rates (NH_3 yield rates) of the 2D C_3N_4-NV, 2D C_3N_4, and bulk C_3N_4. Reproduced with permission [41]. Copyright 2021, Elsevier B.V. (**c**) NH_3 yield of NV-W_2N_3 and W_2N_3 at −0.2 V_{RHE}. (**d**) Synchrotron-based N 1s XPS of W_2N_3 and NV-W_2N_3. Reproduced with permission [42]. Copyright 2019, Wiley–VCH. (**e**) N_2-TPD curves of MoS_2 and MoS_2-800. Reproduced with permission [45]. Copyright 2021, Wiley–VCH.

3.3. Single Atom Catalysts

Single atom catalyst (SAC) synthesis has been regarded as a promising technique for catalyst development. The prepared SACs show outstanding catalytic performances with an extremely high number of active sites and unique electronic properties affecting catalytic pathways [17]. Metal SACs—such as Au, Cu, Fe, and so on—have been proposed and exhibited excellent ENRR performances.

Yongwen Tan et al. prepared Au SACs on nanoporous $MoSe_2$ (Au_{SA}/np-$MoSe_2$) by chemical vapor deposition followed by chemical etching [46]. They compared their ENRR performances with Au nanoparticles on np-$MoSe_2$ (Au_{NPs}/np-$MoSe_2$) and np-$MoSe_2$ alone as shown in Figure 4a,b. At -0.3 V_{RHE} in 0.1 M Na_2SO_4, the Au_{SA}/np-$MoSe_2$ catalyst achieved an FE of 37.82% and an NH_3 production rate of 6.166 μg h^{-1} cm^{-2}, whereas Au_{NPs}/np-$MoSe_2$ and np-$MoSe_2$ exhibited an FE and NH_3 production rate of 11.06% and 1.818 μg h^{-1} cm^{-2} and 11.78% and 0.69 μg h^{-1} cm^{-2}, respectively. Since the Mo dichalcogenides including $MoSe_2$ provide excellent catalytic sites for HER [47], ENRR's representative competitive reaction, the major contribution for NH_3 production enhancement was expected for Au particles. From the XPS spectra of Au 4f, Au_{SA}/np-$MoSe_2$ showed a positively shifted peak attributed to Au^0 compared with Au_{NPs}/np-$MoSe_2$. This indicates that the Au single atom becomes electron-deficient due to a stronger electronic interaction between Au_{SA} and $MoSe_2$, unlike the interaction between Au_{NPs} and $MoSe_2$. Furthermore, Gibbs-free energies calculations for N_2 adsorption on Au additionally supported that the electron-deficient isolated Au single atoms on $MoSe_2$ efficiently inhibited the HER and facilitated N_2 adsorption with the following hydrogenation.

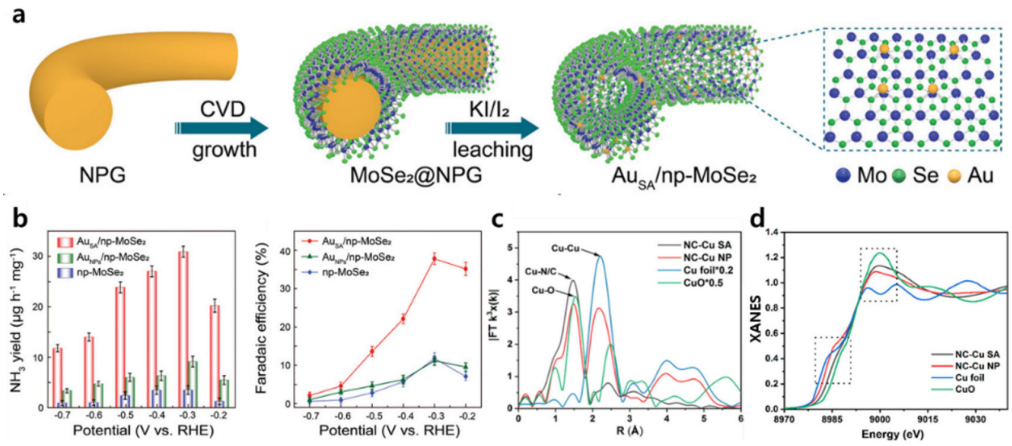

Figure 4. (**a**) Schematic illustration of Au_{SA}/np-$MoSe_2$ preparation process. (**b**) NH_3 production rates (NH_3 yield rates) and FEs of Au_{SA}/np-$MoSe_2$, Au_{NPs}/np-$MoSe_2$ and np-$MoSe_2$. Reproduced with permission [46]. Copyright 2021, Wiley–VCH. (**c**) EXAFS and (**d**) XANES spectra of NC-Cu SA, NC-Cu NP, Cu foil, and CuO. Reproduced with permission [48]. Copyright 2019, American Chemical Society.

Stephen J. Pennycook et al. synthesized Cu single atoms in porous N-doped carbon (NC-Cu SA) using a surfactant-assisted method [48]. As shown in Figure 4c, the presence of a single Cu atom was revealed by EXAFS for Cu K-edge. The NC-Cu SA represents the Cu-N/C peak with a negligible Cu-Cu peak, while NC-Cu NP shows only the Cu-Cu peaks representing the Cu nanoparticle. Furthermore, the single Cu atom in NC-Cu SA represents a positively charged valence state close to Cu^{2+}, unlike Cu particles representing a metallic Cu^0 state in NC-Cu NP as shown in Figure 4d. The electron-deficient Cu single atoms can provide strong N_2 adsorption sites as the first step for the ENRR. The NC-Cu SA catalyst exhibited relatively excellent performance with an FE of 13.8% and an NH_3 production rate of 53.3 μg h^{-1} cm^{-2} at -0.35 V_{RHE} in 0.1 M KOH, whereas NC-Cu NP exhibited an FE of only 4.7% and an NH_3 production rate of 26.8 μg h^{-1} cm^{-2}.

Naturally, NH_3 can be produced by the biological N_2 fixation over nitrogenase enzyme comprising Fe metal with ligands [49]. Xijun Liu et al. synthesized a Fe single atom on N-doped carbon frameworks (Fe_{SA}-NC) inspired by the nitrogenase using the hydrothermal method followed by carbonization [50]. The Fe_{SA}-NC exhibited an FE of 18.6% and an NH_3 production rate of 62.9 μg h^{-1} cm^{-2} at −0.4 V_{RHE} in 0.1 M phosphate buffer solution. The ENRR performance of Fe_{SA}-NC was highly advanced compared to that of Fe_{NPs}-NC. The presence of single Fe atoms on NC was revealed by EXAFS, where the Fe-N bond was shown with a negligible Fe-Fe bond, representing the Fe atom's coordination with the nitrogen atoms but not between the Fe atoms. This result indicates that the Fe-N sites provide an active site for N_2 adsorption and that Fe single atoms contribute to weakening the triple-bond length of N_2 from 1.098 to 1.134 Å.

This subsection demonstrated that SACs have various properties compared to nanoparticle catalysts. For example, SACs change their oxidation state or those of surrounding materials, effectively adsorbing N_2 and weakening the triple bond, consequently enhancing the ENRR.

3.4. Amorphization

Surface amorphization is a promising catalyst engineering technique that partially or completely reduces the crystallinity of regular crystal structures on the catalyst's surface. Compared to highly crystalline structured catalysts, catalysts with reduced crystallinity or an amorphous surface nature can form a lot of defect sites comprising uncoordinated dangling bonds. Furthermore, they can provide lots of sites for reactant adsorption, which is typically the first sluggish step for catalytic reactions [51–53].

Qing jiang et al. prepared amorphous Au NPs on CeO_x-reduced graphite oxide (a-Au/CeO_x-RGO) using the co-reduction method [54]. The CeO_x can reduce the crystallinity of Au and amorphized it. The RGO can provide substrates dispersing the Au NPs. The a-Au/CeO_x-RGO achieved an FE of 10.1% and an NH_3 production rate of 1.66 μg h^{-1} cm^{-2} at −0.2 V_{RHE} in 0.1 M HCl, whereas crystalline Au/RGO only exhibited an FE of 3.67% and a NH_3 production rate of 0.7 μg h^{-1} cm^{-2}. In Au 4f XPS spectra, Au in both a-Au/CeO_x-RGO and c-Au/RGO shows a metallic state. However, in X-ray diffraction (XRD) patterns, unlike c-Au/RGO, a-Au/CeO_x-RGO shows no Au crystalline peak, indicating the amorphous state of Au/CeO_x-RGO. Thus, a-Au/CeO_x-RGO improves ENRR because its amorphous state has an abundance of unsaturated active sites.

Guihua Yu et al. prepared both amorphous and crystalline $Bi_4V_2O_{11}/CeO_2$ using electrospinning with a precursor solution containing different Ce:Bi ratios (1:2 for amorphous and 1:4 for crystalline) and followed calcination [55]. Since the CeO_2 adjusts heat transfer, affecting the neighbor metal's oxidation during calcination, the Ce:Bi ratio can control the crystallinity of $Bi_4V_2O_{11}$. The amorphous $Bi_4V_2O_{11}/CeO_2$ produces an FE of 10.16% and an NH_3 production rate of 46.42 μg h^{-1} cm^{-2} at −0.2 V_{RHE} in 0.1 M HCl, which is about three-times higher FE and a 2.8-fold higher NH_3 production rate for crystalline $Bi_4V_2O_{11}/CeO_2$. The crystalline $Bi_4V_2O_{11}/CeO_2$ showed $Bi_4V_2O_{11}$ of orthorhombic type and CeO_2 cubic type in the XRD pattern, whereas amorphous $Bi_4V_2O_{11}/CeO_2$ showed no obvious $Bi_4V_2O_{11}$ peak. Interestingly, unlike the crystalline $Bi_4V_2O_{11}/CeO_2$ showing only Bi^{3+} and V^{5+}, and dominant lattice O peaks in XPS spectra for Bi 4f, V 2p, and O 1s, respectively, the amorphous $Bi_4V_2O_{11}/CeO_2$ shows Bi^{3+} and Bi^{5+}, V^{5+} and V^{4+}, and an abundance of oxygen vacancy peaks. The additional Bi^{5+} and V^{4+} peaks with oxygen vacancies are observed only for the amorphous sample. This indicates that the amorphous $Bi_4V_2O_{11}/CeO_2$ have intrinsically localized electrons around the defect sites derived from amorphization. Furthermore, they can activate the N_2 adsorption and the first hydrogenation step using a transferred electron and proton.

Ke Chu et al. suggested amorphous FeB_2 nanosheets prepared by a facile reflux method as an electrocatalyst for ENRR [56]. This amorphous FeB_2 exhibited an FE of 16.7% at −0.2 V_{RHE} and an NH_3 production rate of 7.96 μg h^{-1} cm^{-2} at −0.3 V_{RHE} in 0.5 M $LiClO_4$, which are 2- and 3-times higher FE and production rates for crystalline FeB_2, respectively.

This catalytic enhancement's major contribution was revealed by electrochemical active surface area (ECSA) measurements. The amorphous FeB_2 exhibited 1.56-times higher ECSA than crystalline FeB_2, indicating that amorphous FeB_2 has a large active surface area than the crystalline one. Additionally, considering the results of N_2 TPD, the amorphous FeB_2 showed a stronger chemical desorption peak than crystalline FeB_2, implying an enhanced N_2 adsorption ability of amorphous FeB_2 due to the increase in uncoordinated and defective sites in amorphous FeB_2.

These studies support the idea that amorphization is a suitable strategy for increasing the active surface area, number of active sites, effectively providing the appropriate N_2 adsorption strength.

The performance for ENRR depending on strategies for catalyst modification are summarized in Table 1.

Table 1. A brief summary of experimental studies on ENRR using various electrocatalytic engineering strategies.

Catalyst Engineering	Catalyst	Electrolyte	Potential (V_{RHE})	FE (%)	Production Rate ($\mu g\ h^{-1}\ cm^{-2}$)	Refs.
Doping	B,O-CMS	0.1 M HCl	−0.25	5.57	1.92	[15]
	S-CNS	0.1 M Na_2SO_4	−0.7	7.47	1.907	[30]
	Mo-MnO_2 NFS	0.1 M Na_2SO_4	−0.4	12.1	3.46	[33]
	Ag-Cu_{ns}/CP	0.1 M Na_2SO_4	−0.4	20.9	4.56	[34]
	Cl-GDY	0.1 M HCl	−0.45	8.7	10.7	[36]
	N,B-PC	0.1 M HCl	−0.2	10.58	16.4	[37]
	Co/NC_500	0.1 M KOH	−0.1	10.1	10.2	[57]
	PC/Sb/$SbPO_4$	0.1 M HCl	−0.15	31	3.34	[58]
	PC/Sb/$SbPO_4$	0.1 M Na_2SO_4	−0.1	34	2.7	[58]
	Fe,Mo-N/C	0.1 M Na_2SO_4	−0.1	14.2	25.4	[59]
Vacancy	CN/C_{600}	0.1 M HCl	−0.3	16.8	1.93	[16]
	O_v rich TiO_2	0.1 M HCl	−0.12	6.5	3.6	[39]
	2D C_3N_4-NV	0.1 M HCl	−0.3	10.96	178.5	[41]
	NV-W_2N_3	0.1 M KOH	−0.2	11.67	2.332	[42]
	MoS_2-800	0.1 M HCl	−0.35	17.9	9.352	[45]
	C@$CoFe_2O_{4-X}$	0.1 M Na_2SO_4	−0.4	11.65	45.485	[60]
	Ov-TIO2@C/Cu	0.1 M Na_2SO_4	−0.55	6.04	4.025 @ −0.6 V_{RHE}	[61]
	Li-TiO_2(B)	0.5 M $LiClO_4$	−0.4	18.2	0.87	[62]
	CoS_{1-x}	0.05 M H_2SO_4	−0.15	16.5 ± 1.5%	12.1 ± 1.4	[63]
	V_S -MoS_2	0.1 M Na_2SO_4	−0.4	4.58	1.66 @ −0.5 V_{RHE}	[64]
Single atom catalyst	Au_{SA}/np-$MoSe_2$	0.1 M Na_2SO_4	−0.3	37.82	6.166	[46]
	Cu_{sa}-NC	0.1 M KOH	−0.35	13.8	53.3	[48]
	Fe_{sa}-NC	0.1 M phosphate buffer	−0.4	18.6	62.9	[50]
	Ru SAs/N-C	0.05 M H_2SO_4	−0.2	29.6	30.8	[65]
	Y_1/NC	0.1 M HCl	−0.1	12.1	23.2	[66]
	Sc_1/NC	0.1 M HCl	−0.1	11.2	20.4	[66]
	SA Ru-Mo_2CT_X	0.5 M K_2SO_4	−0.3	25.77	12.17	[67]
	W-NO/NC	0.5 M $LiClO_4$	−0.7	8.35	2.524	[68]
	Mn–N–C SAC	0.1 M NaOH	−0.45	32.02	5.36 @ −0.65 V_{RHE}	[69]
	Pt SAs/WO_3	0.1 M K_2SO_4	−0.2	31.1	171.2	[70]
	AuSAs-NDPCs	0.1 M HCl	−0.2	12.3	2.32	[71]
Amorphization	a-Au/CeO_x-RGO	0.1 M HCl	−0.2	10.1	1.66	[54]
	amorphous $Bi_4V_2O_{11}/CeO_2$	0.1 M HCl	−0.2	10.16	46.42	[55]
	amorphous FeB_2 nanosheets	0.5 M $LiClO_4$	−0.3	16.7	7.96	[56]

4. Three-Phase Boundary Engineering

The formation of the three-phase boundary (TPB) of N_2(g)-catalyst(s)-H_2O(l) is critical for the actual ENRR [27,72]. The advanced TPB can effectively suppress HER, the representative competitive reaction, and develop the NH_3 production rate. In this section, strategies for engineering TPB from electrode surface modification to systematic reaction environmental engineering will be discussed in detail.

4.1. Electrode Surface Modification

In typical aqueous ENRR systems, the low N_2 solubility (0.0126 mg·g^{-1}) prevents the effective transfer of N_2, unlike the free accessibility of H_2O, causing a significantly lower N_2 concentration near catalysts than H_2O [20]. It provides an insufficient TPB condition, resulting in an ineffective FE and production rate for ENRR.

One strategy to advance the TPB is modifying the electrode's surface which has a partial hydrophobic nature. Xing Yi Ling et al. suggested coating over the Ag-Au catalyst with the hydrophobic zeolitic imidazolate framework-71 (ZIF-71) (Ag-Au@ZIF-71) by a wet chemical deposition [73]. The distinct characteristics of ZIF-71, having a unique pore structure comprising metal centers and hydrophobic functional groups of dichloroimidazole linkers provides a superhydrophobic barrier, effectively suppressing the free access of H_2O to catalysts [74]. Furthermore, the N_2 molecules can freely diffuse through the ZIF-71 layer and thus be concentrated near the catalyst surface. The relatively reduced H_2O concentration and increased N_2 concentration on catalysts by surface modification with ZIF-71 develop the TPB, effectively resulting in an enhanced ENRR. Ag-Au@ZIF-71 electrode exhibited an advanced FE of 18 ± 4% and an NH_3 production rate of ~0.648 μg h^{-1} cm^{-2} at −2.9 $V_{Ag/AgCl}$ in the solution of 0.2 M $LiCF_3SO_3$ added to ethanol containing dry tetrahydrofuran (TPB), whereas the uncoated Ag-Au electrode showed an FE of only 9% and an NH_3 production rate of 0.1296 μg h^{-1} cm^{-2}. Furthermore, continuous local N_2 saturation led to long-term stability with improved accessibility of N_2 to the catalyst's surface by ZIF-71. The Ag-Au@ZIF-71 represented constant CV features during 45 consecutive potential sweeps between −3 and −0.5 $V_{Ag/AgCl}$. On the other hand, the Ag-Au catalyst showed that the shape of CV was continuously deformed during the consecutive experiments, gradually flattening.

Miao Du et al. proposed a core–shell nanoporous gold (NPG) by encapsulating NPG with ZIF-8 (NPG@ZIF8) as shown in Figure 5a [19]. The 2-methylimidazole linkers comprising ZIF-8 provided a hydrophobic nature and suppressed H_2O accessibility toward NPG catalysts [74]. As shown in Figure 5b, NPG@ZIF-8 showed an FE of 44% and an NH_3 production rate of 22.0 ± 0.3 μg h^{-1} cm^{-2} at −0.6 V_{RHE} in 0.1 M Na_2SO_4, which is 7 times and a 10-fold higher FE and production rate than NPG alone, respectively. The improved ENRR performance mainly originated from ZIF-8 encapsulating NPG by effectively suppressing the competitive HER. NPG@ZIF-8 showed stability with very little change in FE and NH_3 production rate even after 10 consecutive experiments for 2 h each as shown in Figure 5c.

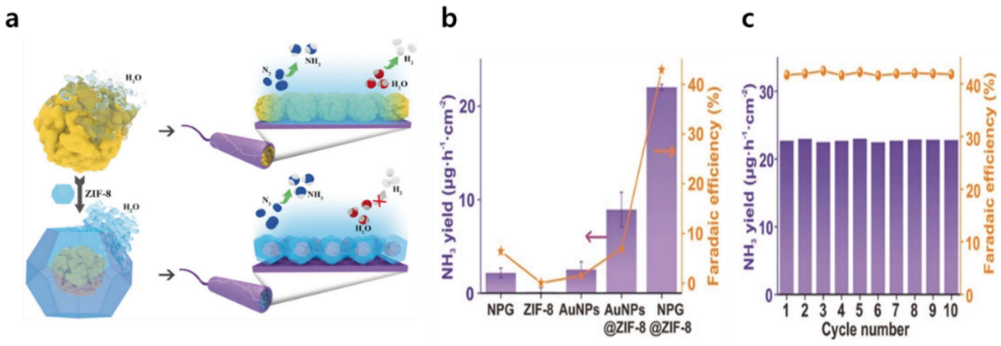

Figure 5. (**a**) Enhancement of N_2 reduction by the NPG@ZIF-8 electrocatalyst. (**b**) Comparison of the FEs and NH_3 production rates (NH_3 yield rates) for the presence and absence of ZIF-8 encapsulation at −0.6 V_{RHE}. (**c**) Stability tests of the NPG@ZIF-8 catalyst at −0.6 V_{RHE}. Reproduced with permission [19]. Copyright 2019, Wiley-VCH.

Even for photoelectrochemical applications, TPB engineering is important for producing NH_3 using N_2 and H_2O with generated photoexcited electrons. Shuangyin Wang et al. proposed a surface modification of a Si-based photocathode using a hydrophobic PTFE porous framework [75]. The photo-excited electrons generated by light absorption

from Si were transferred to Au nanoparticles (Au NP), serving as active sites for ENRR. Since PTFE on Si photocathodes provides a hydrophobic environment originating from strong C-F bonds and resulting in low F polarization and low van der Waals force, H_2O access was dramatically suppressed with accelerating N_2 diffusion toward Au NPs. As a result, the PTFE modified Si photocathode exhibited an FE of 37.8% and an NH_3 production rate 18.9 μg h^{-1} cm^{-2} at −0.2 V_{RHE} in 0.05 M H_2SO_4 with 0.05 M Na_2SO_3 under 1 sun illumination. Its performance was 4- and 1.5-times higher than FE and production rate for pristine Si photocathode with Au NP, respectively.

Furthermore, Pei Kang Shen et al. suggested a way for accumulating N_2 molecules to increase the relative N_2 concentration, resulting in superior TPB for ENRR [76]. They prepared an aerobic-hydrophilic hetero-structured electrocatalyst using ultrathin Bi_5O_7I nanotubes (UP-BOIN) and carbon spheres. The UP-BOIN served as the active sites and showed a highly porous surface structure with a diameter of about 5 nm with a hollow tubular geometry. This morphological trait provides a super-aerophilic nature. Then, the UP-BOIN was combined with the hydrophilic carbon sphere, modified by immersing them in H_2O_2 and 70 wt % H_2SO_4 in series. The combined aerophilic UP-BOIN and hydrophilic carbon sphere can control N_2 accumulation and H_2O accessibility, affecting the superior TPB formation. For example, the 75% UP-BOIN with the 25% carbon sphere sample shows an FE of 6.10% and an NH_3 production rate of 2.286 μg h^{-1} cm^{-2} at −0.4 V_{RHE} in 0.1 M Na_2SO_4. On the other hand, the electrode of 0% UP-BOIN with a 100% carbon sphere shows an FE and a production rate close to 0, indicating that UP-BOIN is a key electrocatalyst providing active sites. Furthermore, the sole UP-BOIN showed a significantly lower 5.19% FE and 0.796 μg h^{-1} cm^{-2} NH_3 production rate compared to the carbon sphere combined UP-BOIN. This indicates that the effective control of reactant concentration, including H_2O, is critical for providing a sufficient TPB for the ENRR.

4.2. Reaction Environmental Engineering

As stated in previous sections, both catalyst modification and TPB advances can play key roles in ENRR development. Thus, it is significantly critical for developing superior TPB via controlling the local concentration of N_2 and H_2O near catalysts. In this section, we will further discuss reaction environmental engineering strategies to develop TPB, including modification of N_2 gas supply, additives in electrolytes, etc.

Kyoung-Shin Choi et al. revealed how local N_2 and H_2O concentrations influence ENRR by suggesting the simple cell modification for N_2 supplying [77]. As shown in Figure 6a, a BiSb alloy-based porous electrode—named the 'regular electrode'—was placed in the typically used setup, where ENRR was performed using dissolved N_2 molecules in H_2O. Additionally, a pseudo-gas diffuse electrode (pseudo-GDE) was proposed by changing the N_2 purging position into the electrode instead of the electrolyte, resulting in a direct N_2 gas supply near the catalyst as shown in Figure 6b. Since they compared the ENRR's performance depending on N_2 supply using perfectly consistent electrodes, the activity benefits from other possible activity-determining factors—such as electrode morphology, catalytic active sites, etc.—are negligible. As shown in Figure 6c, FEs from the pseudo-GDE were significantly altered against the N_2 flow rate because it could change the air pocket's size inside the electrode corresponding to the N_2 concentration. With the increase in the N_2 flow rate up to 100 mL min^{-1}, the FEs increased, representing the N_2 local concentration increase's positive influence on the ENRR. However, over the optimum rate, the efficiencies were decreased due to the significantly limited H_2O supply for catalysts, resulting in reduced TPB sites. At −0.6 V_{RHE}, with the optimal N_2 flow rate, the BiSb regular electrode showed an FE of 1.1% with an NH_3 production rate of 16.29 μg h^{-1} cm^{-2} in 0.5 M borate. On the other hand, the BiSb pseudo-GDE exhibited 5% of FE, a five-fold improvement compared to the regular electrode. Furthermore, the electrode exhibited a highly advanced NH_3 production rate of 66.90 μg h^{-1} cm^{-2}, and the stability was shown through five experimental repetitions in which 5 C passed for each electrolysis.

Xiaofeng Feng et al. proposed a direct N_2 flow cell with a GDE which followed an additional hydrophobic layer modification [20]. Unlike the typically used H-cell which severely suffers from a low concentration of N_2 molecules near the catalyst due to low N_2 solubility (0.0126 $mg \cdot g^{-1}$) in H_2O as shown in Figure 6d, the flow cell with the gas-diffusion layer in Figure 6e can supply sufficient local N_2 concentration via direct humidified N_2 gas fed towards the cathode. Additionally, for the most effective TPB engineering, the developed electrode can be assembled with GDE, catalyst nanoparticles layer deposited on porous and hydrophobic carbon fiber paper, and hydrophobic layer in series as shown in Figure 6e. If the design is experimentally applied, the N_2 gas directly flows and diffuses. Additionally, the protons adjusted by passing the hydrophobic layer are also transferred towards the catalyst layer, which is expected to form a suitable TPB for ENRR by effectively suppressing HER.

Another interesting way to adjust N_2 concentration near catalysts is modifying the composition of electrolytes affecting N_2 solubility. For example, the non-aqueous ionic liquid (IL) can intrinsically inhibit HER because of the significantly low concentration of protons. For example, N_2 solubility is about 20-times higher in trihexyl(tetradecyl) phosphonium tris(pentafluoroethyl) trifluorophosphate, $[P_{6,6,6,14}][eFAP]$ (0.28 $mg \cdot g^{-1}$), representative IL, than the solubility in H_2O (0.0126 $mg \cdot g^{-1}$) at room temperature [78]. Therefore, electrolyte engineering can give an attractive approach for controlling TPB for ENRR.

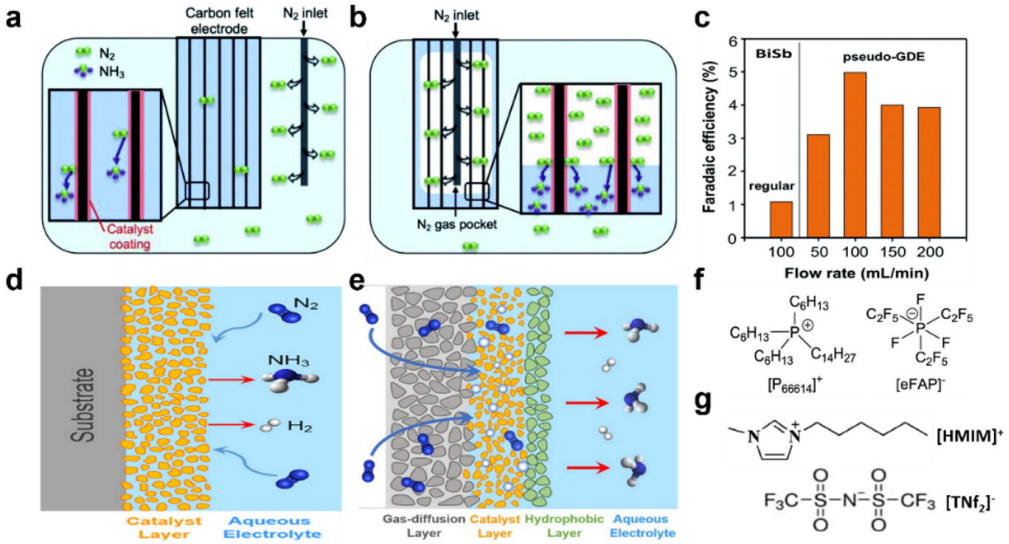

Figure 6. An illustration of (**a**) a regular electrode and (**b**) a pseudo-GDE. (**c**) FEs for $^{15}NH_3$ of BiSb as a regular electrode and as a pseudo-GDE with various $^{15}N_2$ flow rates at -0.6 V_{RHE}. Reproduced with permission [77]. Copyright 2021, Royal Society of Chemistry. Schematic illustration of two types of electrocatalytic interfaces for the ENRR. (**d**) Catalyst(s)-H_2O(l) interface in H-cell. (**e**) Proposed N_2(g)-catalyst(s)-H_2O(l) interface in a flow cell with GDE. Reproduced with permission [20]. Copyright 2020, American Chemical Society. Structure of (**f**) $[P_{6,6,6,14}][eFAP]$ Reproduced with permission [79]. Copyright 2018, American Chemical Society. (**g**) $[HMIM][NTf_2]$. Reproduced with permission [80]. Copyright 2007, American Chemical Society.

Douglas R. MacFalance et al. prepared a Fe electrocatalyst on fluorine-doped tin oxide glass (FTO) substrate by electro-deposition and ENRR was performed using the electrode in the electrolyte of $[P_{6,6,6,14}][eFAP]$ (Figure 6f) [81]. For comparison, ENRR was performed in another ionic liquid 1-hexyl-3-methylimidazolium bis(trifluoromethylsulfonyl)imide $[HMIM][NTf_2]$ (Figure 6g) having a relatively low solubility of 0.017 $mg \cdot g^{-1}$ than $[P_{6,6,6,14}][eFAP]$, showing 0.28 $mg \cdot g^{-1}$ [80]. The differing N_2 solubilities in each electrolyte are due to the interaction between N_2 and $[eFAP]^-$ or $[NTf_2]^-$. According to the DFT calculation, the N_2 molecules can interact with $[eFAP]^-$ in two different ways: N_2 binding with the C_2F_5 group or with

F, showing a binding energy (Eb) of −0.53 and −0.42, respectively. On the other hand, N_2 molecules can make bonds with CF_3 groups of $[NTf_2]^-$ only showing an E_b of −0.16. This indicates that $[eFAP]^-$ provides a much stronger N_2 binding strength than $[NTf_2]^-$, resulting in a more favorable N_2 solubility. This distinct N_2 solubility difference in the two ILs proportionally affects the ENRR. The Fe electrode exhibited an FE of 60 ± 6% in $[P_{6,6,6,14}][eFAP]$, whereas it showed an FE of 0.64% in $[HMIM][NTf_2]$ at −0.8 V_{NHE}.

Zhongfang Chen et al. investigated polyethylene glycol (PEG) additive's effect in 0.05 M H_2SO_4 electrolyte for ENRR using TiO_2 nanoarray electrodes [82]. Even if the majority of the electrolyte is H_2O, a molecular crowding effect formed by hydrogen bonding between H_2O and PEG can significantly suppress H_2O movement. In contrast, since the N_2 molecule is non-polar and its movement was not restricted by the effect, the N_2 molecule can freely move in the electrolyte to reach the active site. As a result, the TiO_2 electrode's FE and NH_3 production rate in the electrolyte with PEG were recorded as 32.13% and 13.6 μg h^{-1} cm^{-2} for −0.3 V_{RHE}. On the other hand, it demonstrated an FE and production rate of only 0.8% and 5.1 μg h^{-1} cm^{-2} without PEG.

In case sufficient protons are present near the catalytic active site, H_2 can be easily adsorbed on electrode surfaces before N_2, leading to a poor ENRR performance. Meanwhile, local H_2O accessibility and its adsorption on active electrode surfaces can be controlled by developing the fundamentals of the electrical double layer (EDL) model [83,84]. For example, if we add additional alkali metal cations to the electrolyte, their hydration is promoted in the beginning. It then suppresses H_2O movement, finally reducing the local H_2O concentration. Furthermore, N_2 absorption strength can be enhanced via the direct adsorption of cations on the surface electrode [85].

An-Xiang Yin et al. investigated the K^+ cation's effect in acidic potassium sulfate for ENRR using Bi catalysts supported on carbon black [85]. They found FEs for ENRR from 9.8% to 66% at −0.6 V_{RHE} depending on the concentration of the K^+ from 0.2 to 1.0 M. Additionally, the NH_3 production rate increased from about 230 to 884 μg h^{-1} cm^{-2}. With the increase in K^+ concentration, the amount of hydrated cations increases. Thus, they can be concentrated in the diffusion layer near the surface at a low potential. The advanced performance is mainly due to proton movement suppression by the hydrated K^+ cations. Therefore, N_2 is first adsorbed to the electrocatalyst's surface and activated. Meanwhile, K^+ directly adsorbed on the electrode can change the Bi electrode's electronic structure, thereby reducing the Gibbs free energy difference for N_2 activation (ΔG_{*NNH}). Thus, by adding the K^+ cation in electrolytes, direct proton adsorption was effectively suppressed and N_2 adsorption and activation was facilitated.

The performances for ENRR depending on strategies for environmental engineering are summarized in Table 2.

Table 2. A brief summary of experimental studies on ENRR using various TPB engineering strategies.

TPB Engineering	Catalyst	Electrolyte	Potential (V_{RHE})	FE (%)	Production Rate (μg h^{-1} cm^{-2})	Refs.
Electrode surface	NPG@ZIF-8	0.1 M Na_2SO_4	−0.6	44	22.0 ± 0.3	[19]
	Ag-Au@ZIF-71	0.2 M $LiCF_3SO_3$ added to ethanol containing dry TPB	−2.9 VAg/AgCl	18 ± 4	0.648	[73]
	AuNp@PTFE	0.05 M H_2SO_4 with 0.05 M Na_2SO_3	−0.2	37.8	18.9	[75]
	UP-BOIN	0.1 M Na_2SO_4	−0.4	6.1	2.286	[76]
Environmental engineering	BiSb(pseudo GDE)	0.5 M borate	−0.6	5	66.9	[77]
	Fe on FTO	[P6,6,6,14][eFAP]	−0.8 V_{NHE}	60 ± 6	0.25	[81]
	TiO_2 nanoarray	PEG in 0.05 M H_2SO_4	−0.3	32.13	13.6	[82]

Table 2. *Cont.*

TPB Engineering	Catalyst	Electrolyte	Potential (V_{RHE})	FE (%)	Production Rate ($\mu g\ h^{-1}\ cm^{-2}$)	Refs.
	nitrogen-doped CNS	0.25 M solution of $LiClO_4$	−1.2	11.5	96	[83]
	Cu	5 M $LiClO_4$	−0.6	12.1 ± 0.8	12.06 ± 2.39	[84]
	Bi on CB	acidic potassiumsulfate (pH 3.5, 1.0 mol L^{-1} of K^+)	−0.6	66	884	[85]
	Pt	gel polymer electrolyte and polyacrylic acid polymer with 6 M KOH	0.5 V (two-electrode system)	0.01%	2.448	[86]
	Nano-Fe/CFC	1 M K_3PO_4	1.0 V~0.0 V	16.68	4.83	[87]

5. Summary and Perspective

NH_3 is an essential precursor for chemicals that are widely used in a variety of industries. Furthermore, it is an important sustainable fuel and media for hydrogen storage. Electrochemical N_2 reduction for NH_3 production (ENRR) has been considered a greatly promising process alternative to the traditional Haber–Bosch process that requires a high-energy input and which emits enormous CO_2 gas. Since the ENRR is performed at an ambient temperature and pressure using N_2 gas and H_2O as a hydrogen resource, it is economically effective and environmentally friendly. Considering those ideal potentials, the scientific community has devoted considerable effort to advancing the performance metrics, including the FE and NH_3 production rate. This review presented ENRR's governing fundamentals, such as thermodynamics, mechanisms, and mass transport. We then introduced strategies for improving its performance.

To design robust electrocatalysts that could provide superior active sites for N_2 adsorption and activation while suppressing HER, defect engineering via heteroatom doping and vacancy formation have been suggested. Furthermore, effective new types of catalysts have been proposed, such as catalysts comprising a single atom grown on a supporter or having an amorphous phase on the surface. These strategies could mainly control electronic structures promoting N_2 adsorption, $*N_2H$, the first intermediate, formation, and further hydrogenation with inhibiting proton adsorption. Meanwhile, to advance the ENRR's performance, not only catalyst engineering but also promising TPB engineering have proved to be critical. Electrode modification with functional layers and reaction environmental modification using direct N_2 gas supply, ionic liquids, and additional cations have been proposed. The desired concentration of N_2 and H_2O near catalysts can be suggested from the modifications, overcoming the major challenges of N_2 mass transport caused by its low solubility in aqueous solutions, and relatively free H_2O accessibility. Recently, the research has also been proposed to improve performance by forming a compact and uniform solid electrolyte interphase (SEI) [88]. Via multiple engineering modifications, the Bi catalysts reported the highest ENRR performance with an FE of 66% and an NH_3 production rate of 884 $\mu g\ h^{-1}\ cm^{-2}$ at −0.6 V_{RHE} in acidic potassium sulfate (pH 3.5, 1.0 mol L^{-1} of K^+).

However, although strategies discussed in this review significantly advanced the ENRR, the performance is still inadequate for the ultimate technical target of practical NH_3 production; namely an FE of 50% and a NH_3 production rate of at least 6120 $\mu g\ h^{-1}\ cm^{-2}$ [12,13]. Therefore, a combination of strategies for catalysts and reaction engineering is necessary for developing ENRR with ultra-high performance. For example, electrochemical CO_2 reductions have similar challenges to ENRR, such as the facile competitive reaction of HER, sluggish first active intermediate formation using transferred electrons and protons, limited TPB caused by imbalanced CO_2, and robust H_2O concentration due to low CO_2 solubility [89–91]. However, their performance was significantly advanced, making them economically feasible by combining robust catalyst developments, environmental reactions,

and environmental engineering, including system and process modification. Benchmarking the signs of progress of CO_2 reduction proves that ENRR could be further improved.

To turn ENRR into a practically available pathway alternative to the Haber–Bosch process, the desired electrocatalysts, environmental conditions, and the other cell components must be sustainable for at least several months. However, those stability issues are barely investigated, even for catalysts tested only for a few hours. Electrocatalysts may decompose due to poisoning, dissolution, and deactivation of active sites [14]. Furthermore, proper reaction environmental conditions can gradually differ compared to the initial state due to varying reactant and product concentrations. Furthermore, the cell components may be decomposed due to unintentional corrosion, pressure changes, etc. Therefore, prolonged stability test periods are highly recommended because they are useful for figuring out the imperfect durability's major origins. If the remaining challenges are successfully solved using the new frontiers suggested above, the ENRR can boost the NH_3 production process, significantly reducing energy consumption and CO_2 emission by replacing the traditional Haber–Bosch process.

Author Contributions: Investigation, conceptualization, and categorization by Y.H.M., N.Y.K. and S.M.K.; Writing and editing by Y.H.M. and N.Y.K.; Funding acquisition, editing, and supervision by Y.J.J. This manuscript was written through contributions of all authors. All authors have read and agreed to the published version of the manuscript.

Funding: This research was funded by the Graduate school of Post Plastic specialization of Korea Environmental Industry & Technology Institute grant funded by the Ministry of Environment of Republic of Korea, the National Research of Korea (NRF) grant (no. 2021R1F1A1063146), and the Korea Institute of Energy Technology Evaluation and Planning (KETEP) and the Ministry of Trade, Industry & Energy (MOTIE) of the Republic of Korea (no. 20202020800330).

Data Availability Statement: The datasets used and analyzed during the current study are available from the corresponding references listed.

Conflicts of Interest: The authors declare no conflict of interest.

References

1. Erisman, J.W.; Sutton, M.A.; Galloway, J.; Klimont, Z.; Winiwarter, W. How a century of ammonia synthesis changed the world. *Nat. Geosci.* **2008**, *1*, 636–639. [CrossRef]
2. Smil, V. Detonator of the population explosion. *Nature* **1999**, *400*, 415. [CrossRef]
3. Chen, J.G.; Crooks, R.M.; Seefeldt, L.C.; Bren, K.L.; Bullock, R.M.; Darensbourg, M.Y.; Holland, P.L.; Hoffman, B.; Janik, M.J.; Jones, A.K.; et al. Beyond fossil fuel-driven nitrogen transformations. *Science* **2018**, *360*, eaar6611. [CrossRef] [PubMed]
4. Bolen, W.P. *Mineral Commodity Summaries 2022*; US Geological Survey: Reston, VA, USA, 2022; p. 202.
5. Wang, K.; Smith, D.; Zheng, Y. Electron-driven heterogeneous catalytic synthesis of ammonia: Current states and perspective. *Carbon Resour. Convers.* **2018**, *1*, 2–31. [CrossRef]
6. Nagaoka, K.; Eboshi, T.; Takeishi, Y.; Tasaki, R.; Honda, K.; Imamura, K.; Sato, K. Carbon-free H_2 production from ammonia triggered at room temperature with an acidic RuO_2/γ-Al_2O_3 catalyst. *Sci. Adv.* **2017**, *3*, e1602747. [CrossRef]
7. Foster, S.L.; Bakovic, S.I.P.; Duda, R.D.; Maheshwari, S.; Milton, R.D.; Minteer, S.D.; Janik, M.J.; Renner, J.N.; Greenlee, L.F. Catalysts for nitrogen reduction to ammonia. *Nat. Catal.* **2018**, *1*, 490–500. [CrossRef]
8. Cui, X.; Tang, C.; Zhang, Q. A review of electrocatalytic reduction of dinitrogen to ammonia under ambient conditions. *Adv. Energy Mater.* **2018**, *8*, 1800369. [CrossRef]
9. Kitano, M.; Inoue, Y.; Yamazaki, Y.; Hayashi, F.; Kanbara, S.; Matsuishi, S.; Yokoyama, T.; Kim, S.-W.; Hara, M.; Hosono, H. Ammonia synthesis using a stable electride as an electron donor and reversible hydrogen store. *Nat. Chem.* **2012**, *4*, 934–940. [CrossRef]
10. MacFarlane, D.R.; Cherepanov, P.V.; Choi, J.; Suryanto, B.H.R.; Hodgetts, R.Y.; Bakker, J.M.; Ferrero Vallana, F.M.; Simonov, A.N. A Roadmap to the ammonia economy. *Joule* **2020**, *4*, 1186–1205. [CrossRef]
11. Smith, C.; Hill, A.K.; Torrente-Murciano, L. Current and future role of Haber–Bosch ammonia in a carbon-free energy landscape. *Energy Environ. Sci.* **2020**, *13*, 331–344. [CrossRef]
12. Kyriakou, V.; Garagounis, I.; Vasileiou, E.; Vourros, A.; Stoukides, M. Progress in the electrochemical synthesis of ammonia. *Catal. Today* **2017**, *286*, 2–13. [CrossRef]
13. Zhao, X.; Hu, G.; Chen, G.-F.; Zhang, H.; Zhang, S.; Wang, H. Comprehensive understanding of the thriving ambient electrochemical nitrogen reduction reaction. *Adv. Mater.* **2021**, *33*, 2007650. [CrossRef]

14. Qing, G.; Ghazfar, R.; Jackowski, S.T.; Habibzadeh, F.; Ashtiani, M.M.; Chen, C.-P.; Smith, M.R.; Hamann, T.W. Recent advances and challenges of electrocatalytic N_2 reduction to ammonia. *Chem. Rev.* **2020**, *120*, 5437–5516. [CrossRef] [PubMed]
15. Tang, M.; Jiang, X.; He, M.; Jiang, N.; Zheng, Q.; Lin, D. B (boron), O (oxygen) dual-doped carbon spheres as a high-efficiency electrocatalyst for nitrogen reduction. *Int. J. Hydrog. Energy* **2021**, *46*, 439–448. [CrossRef]
16. Peng, G.; Wu, J.; Wang, M.; Niklas, J.; Zhou, H.; Liu, C. Nitrogen-defective polymeric carbon nitride nanolayer enabled efficient electrocatalytic nitrogen reduction with high faradaic efficiency. *Nano Lett.* **2020**, *20*, 2879–2885. [CrossRef]
17. Choi, C.; Back, S.; Kim, N.-Y.; Lim, J.; Kim, Y.-H.; Jung, Y. Suppression of hydrogen evolution reaction in electrochemical N_2 reduction using single-atom catalysts: A computational guideline. *ACS Catal.* **2018**, *8*, 7517–7525. [CrossRef]
18. Erkartal, M.; Durandurdu, M. Pressure-induced amorphization of MOF-5: A first principles study. *ChemistrySelect* **2018**, *3*, 8056–8063. [CrossRef]
19. Yang, Y.; Wang, S.-Q.; Wen, H.; Ye, T.; Chen, J.; Li, C.-P.; Du, M. Nanoporous gold embedded ZIF composite for enhanced electrochemical nitrogen fixation. *Angew. Chem. Int. Ed.* **2019**, *58*, 15362–15366. [CrossRef]
20. Hu, L.; Xing, Z.; Feng, X. Understanding the electrocatalytic interface for ambient ammonia synthesis. *ACS Energy Lett.* **2020**, *5*, 430–436. [CrossRef]
21. Chen, X.; Guo, Y.; Du, X.; Zeng, Y.; Chu, J.; Gong, C.; Huang, J.; Fan, C.; Wang, X.; Xiong, J. Atomic structure modification for electrochemical nitrogen reduction to ammonia. *Adv. Energy Mater.* **2020**, *10*, 1903172. [CrossRef]
22. Tavella, F.; Giusi, D.; Ampelli, C. Nitrogen reduction reaction to ammonia at ambient conditions: A short review analysis of the critical factors limiting electrocatalytic performance. *Curr. Opin. Green Sustain. Chem.* **2022**, *35*, 100604. [CrossRef]
23. Bhunia, K.; Sharma, S.K.; Satpathy, B.K.; Pradhan, D. Recent progress in the development of electrocatalysts for the electrochemical N_2 reduction reaction. *Mater. Adv.* **2022**, *3*, 888–917. [CrossRef]
24. Qiao, Z.; Johnson, D.; Djire, A. Challenges and opportunities for nitrogen reduction to ammonia on transitional metal nitrides via Mars-van Krevelen mechanism. *Cell Rep. Phys. Sci.* **2021**, *2*, 100438. [CrossRef]
25. Hawtof, R.; Ghosh, S.; Guarr, E.; Xu, C.; Mohan Sankaran, R.; Renner, J.N. Catalyst-free, highly selective synthesis of ammonia from nitrogen and water by a plasma electrolytic system. *Sci. Adv.* **2019**, *5*, eaat5778. [CrossRef] [PubMed]
26. Yuan, Y.; Tada, S.; Kikuchi, R. Ammonia synthesis using Fe/BZY–RuO_2 catalysts and a caesium dihydrogen phosphate-based electrolyte at intermediate temperatures. *Mater. Adv.* **2021**, *2*, 793–803. [CrossRef]
27. Wang, H.; Chen, Y.; Fan, R.; Chen, J.; Wang, Z.; Mao, S.; Wang, Y. Selective electrochemical reduction of nitrogen to ammonia by adjusting the three-phase interface. *Research* **2019**, *2019*, 1401209. [CrossRef]
28. Lijuan, N.; Ziwen, L.; Guohua, L.; Mengxuan, L.; Xupeng, Z.; Dandan, W.; Li, A.; Dan, Q.; Xiaoming, S.; Xiayan, W.; et al. Surface hydrophobic modification enhanced catalytic performance of electrochemical nitrogen reduction reaction. *Nano Res.* **2022**, *15*, 3886–3893. [CrossRef]
29. Suryanto, B.H.R.; Wang, D.; Azofra, L.M.; Harb, M.; Cavallo, L.; Jalili, R.; Mitchell, D.R.G.; Chatti, M.; MacFarlane, D.R. MoS_2 polymorphic engineering enhances selectivity in the electrochemical reduction of nitrogen to ammonia. *ACS Energy Lett.* **2019**, *4*, 430–435. [CrossRef]
30. Xia, L.; Wu, X.; Wang, Y.; Niu, Z.; Liu, Q.; Li, T.; Shi, X.; Asiri, A.M.; Sun, X. S-doped carbon nanospheres: An efficient electrocatalyst toward artificial N_2 fixation to NH_3. *Small Methods* **2019**, *3*, 1800251. [CrossRef]
31. Xia, L.; Yang, J.; Wang, H.; Zhao, R.; Chen, H.; Fang, W.; Asiri, A.M.; Xie, F.; Cui, G.; Sun, X. Sulfur-doped graphene for efficient electrocatalytic N_2-to-NH_3 fixation. *Chem. Commun.* **2019**, *55*, 3371–3374. [CrossRef]
32. Cheng, S.; Li, C.; Yu, Z.; Sun, Y.; Li, L.; Yang, J. Defective S/N co-doped carbon cloth via a one-step process for effective electroreduction of nitrogen to ammonia. *RSC Adv.* **2020**, *10*, 9814–9823. [CrossRef]
33. Chu, K.; Liu, Y.-p.; Li, Y.-b.; Guo, Y.-l.; Tian, Y.; Zhang, H. Multi-functional Mo-doping in MnO_2 nanoflowers toward efficient and robust electrocatalytic nitrogen fixation. *Appl. Catal. B Environ.* **2020**, *264*, 118525. [CrossRef]
34. Qu, Y.; Dai, T.; Cui, Y.; Zhang, Y.; Wang, Z.; Jiang, Q. Tailoring electronic structure of copper nanosheets by silver doping toward highly efficient electrochemical reduction of nitrogen to ammonia. *Chem. Eng. J.* **2022**, *433*, 133752. [CrossRef]
35. Lv, C.; Qian, Y.; Yan, C.; Ding, Y.; Liu, Y.; Chen, G.; Yu, G. Defect engineering metal-free polymeric carbon nitride electrocatalyst for effective nitrogen fixation under ambient conditions. *Angew. Chem. Int. Ed.* **2018**, *57*, 10246–10250. [CrossRef]
36. Zou, H.; Rong, W.; Long, B.; Ji, Y.; Duan, L. Corrosion-induced Cl-doped ultrathin graphdiyne toward electrocatalytic nitrogen reduction at ambient conditions. *ACS Catal.* **2019**, *9*, 10649–10655. [CrossRef]
37. Ren, J.-T.; Wan, C.-Y.; Pei, T.-Y.; Lv, X.-W.; Yuan, Z.-Y. Promotion of electrocatalytic nitrogen reduction reaction on N-doped porous carbon with secondary heteroatoms. *Appl. Catal. B Environ.* **2020**, *266*, 118633. [CrossRef]
38. Yang, C.; Zhu, Y.; Liu, J.; Qin, Y.; Wang, H.; Liu, H.; Chen, Y.; Zhang, Z.; Hu, W. Defect engineering for electrochemical nitrogen reduction reaction to ammonia. *Nano Energy* **2020**, *77*, 105126. [CrossRef]
39. Han, Z.; Choi, C.; Hong, S.; Wu, T.-S.; Soo, Y.-L.; Jung, Y.; Qiu, J.; Sun, Z. Activated TiO_2 with tuned vacancy for efficient electrochemical nitrogen reduction. *Appl. Catal. B Environ.* **2019**, *257*, 117896. [CrossRef]
40. Morgan, B.J.; Watson, G.W. Intrinsic n-type defect formation in TiO_2: A comparison of rutile and anatase from GGA+U calculations. *J. Phys. Chem. C* **2010**, *114*, 2321–2328. [CrossRef]
41. Zhao, Z.; Long, Y.; Luo, S.; Luo, Y.; Chen, M.; Ma, J. Metal-Free C_3N_4 with plentiful nitrogen vacancy and increased specific surface area for electrocatalytic nitrogen reduction. *J. Energy Chem.* **2021**, *60*, 546–555. [CrossRef]

42. Jin, H.; Li, L.; Liu, X.; Tang, C.; Xu, W.; Chen, S.; Song, L.; Zheng, Y.; Qiao, S.-Z. Nitrogen vacancies on 2D layered W_2N_3: A stable and efficient active site for nitrogen reduction reaction. *Adv. Mater.* **2019**, *31*, 1902709. [CrossRef]
43. Hinnemann, B.; Moses, P.G.; Bonde, J.; Jørgensen, K.P.; Nielsen, J.H.; Horch, S.; Chorkendorff, I.; Nørskov, J.K. Biomimetic hydrogen evolution: MoS_2 nanoparticles as catalyst for hydrogen evolution. *J. Am. Chem. Soc.* **2005**, *127*, 5308–5309. [CrossRef] [PubMed]
44. Liu, J.; Zheng, Y.; Zhu, D.; Vasileff, A.; Ling, T.; Qiao, S.-Z. Identification of pH-dependent synergy on Ru/MoS_2 interface: A comparison of alkaline and acidic hydrogen evolution. *Nanoscale* **2017**, *9*, 16616–16621. [CrossRef] [PubMed]
45. You, M.; Yi, S.; Hou, X.; Wang, Z.; Ji, H.; Zhang, L.; Wang, Y.; Zhang, Z.; Chen, D. High temperature induced S vacancies in natural molybdenite for robust electrocatalytic nitrogen reduction. *J. Colloid Interface Sci.* **2021**, *599*, 849–856. [CrossRef] [PubMed]
46. Chen, D.; Luo, M.; Ning, S.; Lan, J.; Peng, W.; Lu, Y.-R.; Chan, T.-S.; Tan, Y. Single-atom gold isolated onto nanoporous $MoSe_2$ for boosting electrochemical nitrogen reduction. *Small* **2022**, *18*, 2104043. [CrossRef]
47. Zhou, X.; Prikryl, J.; Krbal, M.; Macak, J.M.; Schmuki, P. Molybdenum dichalcogenide nanotube arrays for hydrogen-evolution-reaction catalysis: Synergistic effects of sulfur and selenium in a core-shell tube wall. *Electrochem. Commun.* **2017**, *82*, 112–116. [CrossRef]
48. Zang, W.; Yang, T.; Zou, H.; Xi, S.; Zhang, H.; Liu, X.; Kou, Z.; Du, Y.; Feng, Y.P.; Shen, L.; et al. copper single atoms anchored in porous nitrogen-doped carbon as efficient pH-universal catalysts for the nitrogen reduction reaction. *ACS Catal.* **2019**, *9*, 10166–10173. [CrossRef]
49. Varghese, F.; Kabasakal, B.V.; Cotton, C.A.R.; Schumacher, J.; Rutherford, A.W.; Fantuzzi, A.; Murray, J.W. A low-potential terminal oxidase associated with the iron-only nitrogenase from the nitrogen-fixing bacterium *Azotobacter vinelandii*. *J. Biol. Chem.* **2019**, *294*, 9367–9376. [CrossRef] [PubMed]
50. Lü, F.; Zhao, S.; Guo, R.; He, J.; Peng, X.; Bao, H.; Fu, J.; Han, L.; Qi, G.; Luo, J.; et al. Nitrogen-coordinated single Fe sites for efficient electrocatalytic N_2 fixation in neutral media. *Nano Energy* **2019**, *61*, 420–427. [CrossRef]
51. Hu, F.; Wang, H.; Zhang, Y.; Shen, X.; Zhang, G.; Pan, Y.; Miller, J.T.; Wang, K.; Zhu, S.; Yang, X.; et al. Designing highly efficient and long-term durable electrocatalyst for oxygen evolution by coupling B and P into amorphous porous NiFe-based material. *Small* **2019**, *15*, 1901020. [CrossRef]
52. Kim, J.S.; Kim, B.; Kim, H.; Kang, K. Recent progress on multimetal oxide catalysts for the oxygen evolution reaction. *Adv. Energy Mater.* **2018**, *8*, 1702774. [CrossRef]
53. Nsanzimana, J.M.V.; Peng, Y.; Xu, Y.Y.; Thia, L.; Wang, C.; Xia, B.Y.; Wang, X. An efficient and earth-abundant oxygen-evolving electrocatalyst based on amorphous metal borides. *Adv. Energy Mater.* **2018**, *8*, 1701475. [CrossRef]
54. Li, S.-J.; Bao, D.; Shi, M.-M.; Wulan, B.-R.; Yan, J.-M.; Jiang, Q. Amorphizing of Au nanoparticles by CeO_x–RGO hybrid support towards highly efficient electrocatalyst for N_2 reduction under ambient conditions. *Adv. Mater.* **2017**, *29*, 1700001. [CrossRef]
55. Lv, C.; Yan, C.; Chen, G.; Ding, Y.; Sun, J.; Zhou, Y.; Yu, G. An amorphous noble-metal-free electrocatalyst that enables nitrogen fixation under ambient conditions. *Angew. Chem. Int. Ed.* **2018**, *57*, 6073–6076. [CrossRef]
56. Chu, K.; Gu, W.; Li, Q.; Liu, Y.; Tian, Y.; Liu, W. Amorphization activated FeB_2 porous nanosheets enable efficient electrocatalytic N_2 fixation. *J. Energy Chem.* **2021**, *53*, 82–89. [CrossRef]
57. Gao, Y.; Han, Z.; Hong, S.; Wu, T.; Li, X.; Qiu, J.; Sun, Z. ZIF-67-derived cobalt/nitrogen-doped carbon composites for efficient electrocatalytic N_2 reduction. *ACS Appl. Energy Mater.* **2019**, *2*, 6071–6077. [CrossRef]
58. Liu, X.; Jang, H.; Li, P.; Wang, J.; Qin, Q.; Kim, M.G.; Li, G.; Cho, J. Antimony-based composites loaded on phosphorus-doped carbon for boosting faradaic efficiency of the electrochemical nitrogen reduction reaction. *Angew. Chem. Int. Ed.* **2019**, *58*, 13329–13334. [CrossRef]
59. Ye, W.; Yang, Y.; Arif, M.; Yang, S.; Fang, X.; Mushtaq, M.A.; Chen, X.; Yan, D. Fe, Mo–N/C hollow porous nitrogen-doped carbon nanorods as an effective electrocatalyst for N_2 reduction reaction. *ACS Sustain. Chem. Eng.* **2020**, *8*, 15946–15952. [CrossRef]
60. Wang, C.; Gu, L.-L.; Qiu, S.-Y.; Gao, J.; Zhang, Y.-C.; Wang, K.-X.; Zou, J.-J.; Zuo, P.-J.; Zhu, X.-D. Modulating $CoFe_2O_4$ nanocube with oxygen vacancy and carbon wrapper towards enhanced electrocatalytic nitrogen reduction to ammonia. *Appl. Catal. B Environ.* **2021**, *297*, 120452. [CrossRef]
61. Li, Y.; Liang, Y.; Li, H.; Wang, B.; You, H.; Wang, Y.; Cao, Y.; Dai, W.; Gao, F. The surface engineering of MOF-derived titanium oxide–carbon multifunctional composite catalyst for efficient electrochemical nitrogen reduction. *Appl. Surf. Sci.* **2021**, *570*, 151257. [CrossRef]
62. Zhao, R.; Wang, G.; Mao, Y.; Bao, X.; Wang, Z.; Wang, P.; Liu, Y.; Zheng, Z.; Dai, Y.; Cheng, H.; et al. Li-intercalation boosted oxygen vacancies enable efficient electrochemical nitrogen reduction on ultrathin TiO_2 nanosheets. *Chem. Eng. J.* **2022**, *430*, 133085. [CrossRef]
63. Li, C.; Xu, R.; Ma, S.; Xie, Y.; Qu, K.; Bao, H.; Cai, W.; Yang, Z. Sulfur vacancies in ultrathin cobalt sulfide nanoflowers enable boosted electrocatalytic activity of nitrogen reduction reaction. *Chem. Eng. J.* **2021**, *415*, 129018. [CrossRef]
64. Ma, C.; Zhai, N.; Liu, B.; Yan, S. Defected MoS2: An efficient electrochemical nitrogen reduction catalyst under mild conditions. *Electrochim. Acta* **2021**, *370*, 137695. [CrossRef]
65. Geng, Z.; Liu, Y.; Kong, X.; Li, P.; Li, K.; Liu, Z.; Du, J.; Shu, M.; Si, R.; Zeng, J. Achieving a record-high yield rate of 120.9 for N_2 electrochemical reduction over Ru single-atom catalysts. *Adv. Mater.* **2018**, *30*, 1803498. [CrossRef]
66. Liu, J.; Kong, X.; Zheng, L.; Guo, X.; Liu, X.; Shui, J. Rare earth single-atom catalysts for nitrogen and carbon dioxide reduction. *ACS Nano* **2020**, *14*, 1093–1101. [CrossRef]

67. Peng, W.; Luo, M.; Xu, X.; Jiang, K.; Peng, M.; Chen, D.; Chan, T.-S.; Tan, Y. Spontaneous atomic ruthenium doping in Mo_2CT_X MXene defects enhances electrocatalytic activity for the nitrogen reduction reaction. *Adv. Energy Mater.* **2020**, *10*, 2001364. [CrossRef]
68. Gu, Y.; Xi, B.; Tian, W.; Zhang, H.; Fu, Q.; Xiong, S. Boosting selective nitrogen reduction via geometric coordination engineering on single-tungsten-atom catalysts. *Adv. Mater.* **2021**, *33*, 2100429. [CrossRef]
69. Wang, X.; Wu, D.; Liu, S.; Zhang, J.; Fu, X.-Z.; Luo, J.-L. Folic acid self-assembly enabling manganese single-atom electrocatalyst for selective nitrogen reduction to ammonia. *Nano-Micro Lett.* **2021**, *13*, 125. [CrossRef] [PubMed]
70. Hao, R.; Sun, W.; Liu, Q.; Liu, X.; Chen, J.; Lv, X.; Li, W.; Liu, Y.-p.; Shen, Z. Efficient electrochemical nitrogen fixation over isolated Pt sites. *Small* **2020**, *16*, 2000015. [CrossRef]
71. Sahoo, S.K.; Heske, J.; Antonietti, M.; Qin, Q.; Oschatz, M.; Kühne, T.D. Electrochemical N_2 reduction to ammonia using single Au/Fe atoms supported on nitrogen-doped porous carbon. *ACS Appl. Energy Mater.* **2020**, *3*, 10061–10069. [CrossRef] [PubMed]
72. Lai, F.; Zong, W.; He, G.; Xu, Y.; Huang, H.; Weng, B.; Rao, D.; Martens, J.A.; Hofkens, J.; Parkin, I.P.; et al. N_2 electroreduction to NH_3 by selenium vacancy-rich $ReSe_2$ catalysis at an abrupt interface. *Angew. Chem. Int. Ed.* **2020**, *59*, 13320–13327. [CrossRef]
73. Lee, H.K.; Koh, C.S.L.; Lee, Y.H.; Liu, C.; Phang, I.Y.; Han, X.; Tsung, C.-K.; Ling, X.Y. Favoring the unfavored: Selective electrochemical nitrogen fixation using a reticular chemistry approach. *Sci. Adv.* **2018**, *4*, eaar3208. [CrossRef]
74. Zhang, K.; Lively, R.P.; Dose, M.E.; Brown, A.J.; Zhang, C.; Chung, J.; Nair, S.; Koros, W.J.; Chance, R.R. Alcohol and water adsorption in zeolitic imidazolate frameworks. *Chem. Commun.* **2013**, *49*, 3245–3247. [CrossRef]
75. Zheng, J.; Lyu, Y.; Qiao, M.; Wang, R.; Zhou, Y.; Li, H.; Chen, C.; Li, Y.; Zhou, H.; Jiang, S.P.; et al. Photoelectrochemical synthesis of ammonia on the aerophilic-hydrophilic heterostructure with 37.8% efficiency. *Chem* **2019**, *5*, 617–633. [CrossRef]
76. Liu, Y.; Huang, B.; Chen, X.; Tian, Z.; Zhang, X.; Tsiakaras, P.; Shen, P.K. Electrocatalytic production of ammonia: Biomimetic electrode–electrolyte design for efficient electrocatalytic nitrogen fixation under ambient conditions. *Appl. Catal. B Environ.* **2020**, *271*, 118919. [CrossRef]
77. Jang, Y.J.; Evans, T.A.; Samanta, B.; Zeng, K.; Toroker, M.C.; Choi, K.-S. A comparative study of Bi, Sb, and BiSb for electrochemical nitrogen reduction leading to a new catalyst design strategy. *J. Mater. Chem. A* **2021**, *9*, 20453–20465. [CrossRef]
78. Stevanovic, S.; Costa Gomes, M.F. Solubility of carbon dioxide, nitrous oxide, ethane, and nitrogen in 1-butyl-1-methylpyrrolidinium and trihexyl(tetradecyl)phosphonium tris(pentafluoroethyl)trifluorophosphate (eFAP) ionic liquids. *J. Chem. Thermodyn.* **2013**, *59*, 65–71. [CrossRef]
79. Kang, C.S.M.; Zhang, X.; MacFarlane, D.R. Synthesis and physicochemical properties of fluorinated ionic liquids with high nitrogen gas solubility. *J. Phys. Chem. C* **2018**, *122*, 24550–24558. [CrossRef]
80. Anderson, J.L.; Dixon, J.K.; Brennecke, J.F. Solubility of CO_2, CH_4, C_2H_6, C_2H_4, O_2, and N_2 in 1-Hexyl-3-methylpyridinium Bis(trifluoromethylsulfonyl)imide: Comparison to other ionic liquids. *Acc. Chem. Res.* **2007**, *40*, 1208–1216. [CrossRef] [PubMed]
81. Zhou, F.; Azofra, L.M.; Ali, M.; Kar, M.; Simonov, A.N.; McDonnell-Worth, C.; Sun, C.; Zhang, X.; MacFarlane, D.R. Electro-synthesis of ammonia from nitrogen at ambient temperature and pressure in ionic liquids. *Energy Environ. Sci.* **2017**, *10*, 2516–2520. [CrossRef]
82. Guo, Y.; Gu, J.; Zhang, R.; Zhang, S.; Li, Z.; Zhao, Y.; Huang, Z.; Fan, J.; Chen, Z.; Zhi, C. Molecular crowding effect in aqueous electrolytes to suppress hydrogen reduction reaction and enhance electrochemical nitrogen reduction. *Adv. Energy Mater.* **2021**, *11*, 2101699. [CrossRef]
83. Song, Y.; Johnson, D.; Peng, R.; Hensley, D.K.; Bonnesen, P.V.; Liang, L.; Huang, J.; Yang, F.; Zhang, F.; Qiao, R.; et al. A physical catalyst for the electrolysis of nitrogen to ammonia. *Sci. Adv.* **2018**, *4*, e1700336. [CrossRef]
84. Guha, A.; Narayanaru, S.; Kaley, N.M.; Krishna Rao, D.; Mondal, J.; Narayanan, T.N. Mechanistic insight into high yield electrochemical nitrogen reduction to ammonia using lithium ions. *Mater. Today Commun.* **2019**, *21*, 100700. [CrossRef]
85. Hao, Y.-C.; Guo, Y.; Chen, L.-W.; Shu, M.; Wang, X.-Y.; Bu, T.-A.; Gao, W.-Y.; Zhang, N.; Su, X.; Feng, X.; et al. Promoting nitrogen electroreduction to ammonia with bismuth nanocrystals and potassium cations in water. *Nat. Catal.* **2019**, *2*, 448–456. [CrossRef]
86. Sheets, B.L.; Botte, G.G. Electrochemical nitrogen reduction to ammonia under mild conditions enabled by a polymer gel electrolyte. *Chem. Commun.* **2018**, *54*, 4250–4253. [CrossRef]
87. Zhang, Q.; Liu, B.; Yu, L.; Bei, Y.; Tang, B. Synergistic promotion of the electrochemical reduction of nitrogen to ammonia by phosphorus and potassium. *ChemCatChem* **2020**, *12*, 334–341. [CrossRef]
88. Li, S.; Zhou, Y.; Li, K.; Saccoccio, M.; Sažinas, R.; Andersen, S.Z.; Pedersen, J.B.; Fu, X.; Shadravan, V.; Chakraborty, D.; et al. Electrosynthesis of ammonia with high selectivity and high rates via engineering of the solid-electrolyte interphase. *Joule* **2022**, *6*, 1–19. [CrossRef]
89. Bagger, A.; Ju, W.; Varela, A.S.; Strasser, P.; Rossmeisl, J. Electrochemical CO_2 reduction: A classification problem. *ChemPhysChem* **2017**, *18*, 3266–3273. [CrossRef] [PubMed]
90. Jones, J.-P.; Prakash, G.K.S.; Olah, G.A. Electrochemical CO_2 reduction: Recent advances and current trends. *Isr. J. Chem.* **2014**, *54*, 1451–1466. [CrossRef]
91. Zhang, B.; Jiang, Y.; Gao, M.; Ma, T.; Sun, W.; Pan, H. Recent progress on hybrid electrocatalysts for efficient electrochemical CO_2 reduction. *Nano Energy* **2021**, *80*, 105504. [CrossRef]